Delft University of Technology

Document Version
Final published version

Licence
CC BY

Citation (APA)
Paternina, M. R. A., Rios, G. L., Villalobos, P. M., Zamora-Mendez, A., Parajuli, A., Castrillón Franco, M. C., Mejia-Ruiz, G. E., Velazquez-Ibañez, A., Segundo Sevilla, F. R., & Korba, P. (2026). Power Oscillation Damping Controller Powered by Data-Assisted Dominant Modal Decomposition. *Energies*, *19*(18), Article 4433. https://doi.org/10.3390/en19184433

Important note
To cite this publication, please use the final published version (if applicable).
Please check the document version above.

Copyright
In case the licence states “Dutch Copyright Act (Article 25fa)”, this publication was made available Green Open Access via the TU Delft Institutional Repository pursuant to Dutch Copyright Act (Article 25fa, the Taverne amendment). This provision does not affect copyright ownership.
Unless copyright is transferred by contract or statute, it remains with the copyright holder.

Sharing and reuse
Other than for strictly personal use, it is not permitted to download, forward or distribute the text or part of it, without the consent of the author(s) and/or copyright holder(s), unless the work is under an open content license such as Creative Commons.

Takedown policy
Please contact us and provide details if you believe this document breaches copyrights.
We will remove access to the work immediately and investigate your claim.

This work is downloaded from Delft University of Technology.

energies

MDPI

Article

Power Oscillation Damping Controller Powered by Data-Assisted Dominant Modal Decomposition

Mario R. Arrieta Paternina [1,2], Gilberto Lopez Rios [3], Pablo Moreno Villalobos [3], Alejandro Zamora-Mendez [4], Amrit Parajuli [2], Camila Castrillón-Franco [5], Gabriel E. Mejia-Ruiz [6], Alfredo Velazquez-Ibañez [2], Felix Rafael Segundo Sevilla [2] and Petr Korba [2,*]

1 Department of Electrical Engineering, National Autonomous University of Mexico, Mexico City 04510, Mexico; mra.paternina@fi-b.unam.mx
2 Electric Power Systems and Smart Grids Group, Institute of Energy Systems and Fluid Engineering (IEFE), ZHAW, 8400 Winterthur, Switzerland; amrit.parajulee@gmail.com (A.P.); vela@zhaw.ch (A.V.-I.); segu@zhaw.ch (F.R.S.S.)
3 Centre for Research and Advanced Studies of Mexico (CINVESTAV), Campus Guadalajara, Zapopan 45019, Mexico; gilberto.lopez@cinvestav.mx (G.L.R.); pablo.moreno@cinvestav.mx (P.M.V.)
4 Electrical Engineering Faculty, Universidad Michoacana de San Nicolás de Hidalgo, Morelia 58030, Mexico; azamoram@umich.mx
5 Intelligent Electrical Power Grids, University of Technology (TU Delft), 2628 CD Delft, The Netherlands; mcastrillonfra@tudelft.nl
6 Electrical and Electronics Engineering School, Universidad del Valle, Cali 760032, Colombia; gabriel.mejia.ruiz@correounivalle.edu.co
* Correspondence: korb@zhaw.ch

Abstract

This paper focuses on deriving power-system linear models directly from collected PMU data with the aim of feeding a wide-area damping controller (WADC) architecture. To this end, a data-assisted dominant modal realization in state space is derived from frequency-response data, impulse-response data, and the retained impulse dynamic subspace, enabling WADC synthesis without requiring a full phenomenological network model. Then, a discrete-time linear quadratic Gaussian (LQG) structure is synthesized on the identified dominant modal realization, combining damping action with reconstruction of reduced states from WAMS measurements. Finally, the symbiosis between the proposed realization and the controller is validated on the Kundur and New England–New York power networks by using modal displacement and nonlinear post-fault simulations, demonstrating coordinated damping through selected AVR supplementary inputs.

Keywords: wide-area damping controller; dominant modal realization; power-system linear model; system identification; linear quadratic Gaussian

Check for updates

Academic Editor: Krzysztof Górecki

Received: 7 August 2026
Revised: 2 September 2026
Accepted: 8 September 2026
Published: 19 September 2026

Copyright: © 2026 by the authors. Licensee MDPI, Basel, Switzerland. This article is an open access article distributed under the terms and conditions of the Creative Commons Attribution (CC BY) license.

1. Introduction

Low-frequency electromechanical oscillations remain a limiting factor for the secure operation of large interconnected power systems. Inter-area oscillations are particularly critical because they involve coherent groups of generators swinging against each other through weak transmission corridors. When insufficiently damped, these modes restrict power transfer, reduce stability margins, and compromise grid dynamic security [1,2]. Their relevance has increased in modern networks, where operating points vary more frequently and the coexistence of synchronous machines, renewable generation, and power-electronic interfaces modifies the modal structure of the system.

Power-system stabilizers (PSSs) acting through the automatic voltage regulators (AVRs) of synchronous generators provide the conventional first damping layer. This structure is effective for several local modes, but local feedback may exhibit limited observability of inter-area dynamics [3]. A local controller can therefore be inadequate when the critical mode is observable in one area and controllable from another [2,4]. This limitation motivates the use of wide-area damping controllers (WADCs), where remote measurements coordinate supplementary control actions across selected devices or generators [5].

The deployment of phasor measurement units (PMUs) and wide-area measurement systems (WAMSs) has enabled WADC schemes based on synchronized electrical and electromechanical measurements. These signals provide global information about inter-area dynamics and can reduce the control effort required to obtain a given damping effect when compared with purely local feedback [2,6]. Wide-area control has been implemented through generator excitation systems, flexible AC transmission system devices, voltage-source converters, high-voltage DC links, energy storage systems, wind turbine converters, and hydropower governors [7–9]. Nevertheless, WADC design remains challenging because remote feedback is affected by measurement noise, latency, packet losses, operating-point variation, and actuator saturation.

Linear quadratic Gaussian (LQG) control is a suitable framework for WADC design because it combines an optimal state-feedback regulator with a Kalman estimator. Early LQG/LTR-based controllers showed that output-feedback structures can improve inter-area damping when suitable reduced plants are available [10]. Subsequent studies extended LQG-based WADC design to discrete-time implementations, communication impairments, energy-storage-based actuation, hydropower plants, and adaptive wide-area controllers [4,7–9]. Observer-based strategies have also been introduced to estimate modal or functional feedback signals that cannot be directly measured by PMU devices [6,11]. These developments confirm the relevance of output-feedback optimal control for inter-area damping, but they still require a control-oriented reduced model that is accurate enough for synthesis, interpretable in modal terms, and compatible with available WAMS channels.

A central difficulty is that many WADC designs require a linearized power-system model with reliable topology, parameters, operating conditions, and actuator representations. In practical systems, this information may be incomplete, uncertain, or outdated. Data-driven and measurement-based WADC strategies address this limitation by exploiting PMU/WAMS data to identify modal properties or control-oriented models directly from measurements [2,12]. However, fully model-free or black-box methods may depend strongly on the selected measurement set, require online re-identification or pre-tuning, and provide limited physical interpretation of the identified small-signal dynamics. Accordingly, the contribution of this work lies in establishing a data-assisted pathway from AVR-to-WAMS frequency-response data to a reduced dominant modal realization tailored for wide-area damping control. The proposed formulation preserves an explicit correspondence between the identified electromechanical dynamics, the selected actuation and measurement channels, and the state-space matrices required for discrete-time output-feedback synthesis. This connection enables the dominant dynamics extracted from frequency-response data to be directly exploited within the LQG-WADC design framework.

This paper addresses this gap by proposing a data-assisted dominant modal decomposition (DMD) to feed a power oscillation damping controller. In this work, DMD denotes a dominant modal decomposition derived from frequency-response functions, impulse-response functions, Green function representations, and a retained impulse dynamic subspace. It does not refer to a snapshot-only dynamic mode decomposition algorithm. The proposed framework identifies the dominant electromechanical dynamics from controlled AVR probing experiments and the associated multichannel WAMS responses, constructs a

reduced state-transition map in the retained impulse-dynamic coordinates, and converts this map into a control-oriented multiple-input multiple-output realization by projecting the selected AVR actuation channels and WAMS measurement channels onto the retained dynamic subspace.

On top of this reduced realization, a discrete-time LQG-WADC is synthesized. The linear quadratic regulator computes the supplementary damping action, whereas the linear quadratic estimator reconstructs the reduced dominant-modal coordinates from the available WAMS measurements. The resulting command is applied as an additional signal to selected AVR reference inputs. This structure preserves a direct link between the identified dominant modes, the measurement channels used by the estimator, the performance variables penalized in the regulator, and the physical actuation path in the nonlinear power-system model.

The proposed methodology is evaluated on the two-area Kundur system and the New England–New York power system (NEPS-NYPS) 68-bus system through closed-loop modal displacement and nonlinear post-fault simulations. The Kundur case evaluates coordinated supplementary action through four AVR channels, whereas the NEPS-NYPS case examines the same architecture through sixteen AVR channels and multiple inter-area corridors. Additional scenarios assess the reported sensitivity to communication delays and the modified NEPS-NYPS configuration containing wind power plants and HVDC links. These studies quantify performance under the considered conditions and do not constitute a general robustness guarantee for arbitrary operating-point, topology changes, or communication problems.

The main contributions of this paper are as follows:

- A data-assisted dominant modal realization is derived from frequency-response data, impulse-response data, and the retained impulse dynamic subspace, enabling WADC synthesis without requiring a full phenomenological network model.
- A discrete-time LQG-WADC is synthesized on the identified dominant modal realization, combining LQR-based damping action with LQE-based reconstruction of reduced coordinates from WAMS measurements.
- The proposed controller is validated on the Kundur and NEPS-NYPS benchmarks using modal displacement and nonlinear post-fault simulations, demonstrating coordinated damping through selected AVR supplementary inputs.

The remainder of the paper presents the dominant-modal modeling procedure, the LQG-WADC synthesis, and the modal and nonlinear post-fault validation on the selected benchmarks.

2. Frequency Data-Based Dominant Decomposition Linear Models

This section adopts the power-system linear model derivation by using the dominant mode decomposition framework adapted to multi-machine power networks. The frequency measurements are assembled with direct point-to-point frequency response functions (FRFs), including all spatio-temporal behaviors that are correlated by

$$\mathbf{H}_{q,i}(\omega_k) = \frac{\mathbf{Y}_{q,i}(\omega_k)}{\mathbf{U}_i(\omega_k)} \tag{1}$$

where all outputs $\mathbf{Y}_{q,i}(\omega_k)$ and their corresponding inputs $\mathbf{U}_i(\omega_k)$ result from applying the fast Fourier transform (fft) to the discrete-time signals $y_{q,i}$ and u_i, respectively, evaluated

at the discrete frequency spectral points $\omega_k = 2\pi f_k$. The excitation signals are defined as chirp functions as in [13]:

$$u_i(t) = \alpha_i \sin\left(\frac{2\pi f_s(r_f^t - 1)}{\ln(r_f)}\right) \tag{2}$$

$$r_f = \left(\frac{f_e}{f_s}\right)^{1/T} \tag{3}$$

where the amplitude is denoted by α_i, the lasting time is represented by T, and f_s and f_e are, respectively, the low and high frequencies of the chirp signal. Then, each point in (1) is mapped into a matrix function $\mathbf{H}(\omega)$, considering N_m non-proportional damping modes (λ), as follows [14]:

$$\mathbf{H}(\omega) = [\mathbf{H}_{q,i}(\omega)] = \sum_{m=1}^{N_m} \frac{Q_m \mathbf{v}_m \mathbf{w}'_m}{i\omega - \lambda_m} + \frac{\bar{Q}_m \bar{\mathbf{v}}_m \mathbf{w}_m^H}{i\omega - \bar{\lambda}_m}, \tag{4}$$

where Q_m stands for the scaling factor, $\mathbf{v}_m$ represents the mode shapes, and $\mathbf{w}_m$ is the modal participation vectors.

Notice that matrix $\mathbf{H}_{q,i}(\omega) = [H_{q,i;k,m}(\omega)]$ for all $q = 1, \cdots, p$ and $i = 1, \cdots, n$ corresponds to the frequency response functions (FRFs). Then, the impulse response functions (IRFs) are required to assemble the impulse dynamic subspace, as follows [14]:

$$\mathbf{h}(\theta) = \mathcal{F}^{-1}[\mathbf{H}(\omega)], \quad \text{and} \quad \mathbf{h}_\mathrm{d}(\theta) = \mathcal{F}^{-1}[\mathbf{H}_\mathrm{d}(\omega)], \tag{5}$$

where $\mathbf{h}(\theta) : [0, \infty] \to \mathbb{R}^{p \times n}$ and $\mathbf{h}_\mathrm{d}(\theta) : [0, \infty] \to \mathbb{R}^{n \times n}$.

2.1. Continuous Time

Dynamic systems can be represented in integral form, avoiding kinematic initial conditions (ICs) and replacing them with dynamic past force evolution $\mathbf{F}^- = \mathbf{F}(t)(t \in (-\infty, 0))$. This forces the system to achieve the actual IC for a fixed $t = 0$. The mapping of free oscillatory dynamics can be described by the Green function $\mathbf{G}$ in the form [14]

$$\mathbf{x}(t + \theta) = \int_0^\infty \mathbf{G}(\theta, \vartheta)\mathbf{F}^-(t - \vartheta)\mathrm{d}\vartheta. \tag{6}$$

where the system is restricted to its direct dynamics presented by the direct Green function $\mathbf{G}_\mathrm{d}(\theta, \vartheta) = \mathbf{h}_\mathrm{d}(\theta + \vartheta)$, and the operator $\mathbf{G}$ can be rewritten in a reduced representation by using singular value decomposition (SVD), facilitating the identification of all subsystems in (6) and assuming a perfect representation of $\mathbf{G}$ [14]:

$$\mathbf{G}_\mathrm{d}(\theta, \vartheta) = \sum_{k=1}^{\infty} \sigma_k \mathbf{V}_{\mathrm{d},k}(\theta)\mathbf{W}_k^\mathrm{H}(\vartheta), \tag{7}$$

where σ_k are singular values. The left- and right-singular functions are unitary $\mathbf{V}_{\mathrm{d},k}(\theta)$, $\mathbf{W}_k(\vartheta) : [0, \infty] \to \mathbb{C}$, $\mathbf{W}_{\mathrm{d},k}(\theta) = \mathbf{W}_k(\theta)$, and $\mathbf{G}_\mathrm{d}$ can be derived by taking an appropriate singular set $\mathcal{M}(|\mathcal{M}| = M$, typically $\mathcal{M} = \{1, 2, \ldots, M\})$ as $\tilde{\mathbf{V}}_\mathrm{d}(\theta) = \mathrm{row}_{k \in \mathcal{M}} \mathbf{V}_{\mathrm{d},k}(\theta)$ and $\tilde{\mathbf{W}}(\vartheta) = \mathrm{row}_{k \in \mathcal{M}} \mathbf{W}_k(\vartheta)$. Thus, a direct solution can be rewritten by the introduction of the impulse dynamic subspace based on the M-left impulse response functions, such that [14]

$$\mathbf{x}_\mathrm{d}(t + \theta) = \tilde{\mathbf{V}}_\mathrm{d}(\theta)\mathbf{q}(t). \tag{8}$$

This has the following dynamics:

$$\dot{\mathbf{x}}_{\mathrm{d}}(t+\theta) = \tilde{\mathbf{V}}_{\mathrm{d}}(\theta)\dot{\mathbf{q}}(t) \quad \text{and} \quad \dot{\mathbf{x}}_{\mathrm{d}}(t+\theta) = \tilde{\mathbf{V}}'_{\mathrm{d}}(\theta)\mathbf{q}(t). \tag{9}$$

Then, the system matrix can be derived by using the unitary condition of the set of M left impulse response functions, as

$$\dot{\mathbf{q}}(t) = \langle \tilde{\mathbf{V}}_{\mathrm{d}}(\theta), \tilde{\mathbf{V}}'_{\mathrm{d}}(\theta) \rangle \mathbf{q}(t) \quad \Rightarrow \quad \dot{\mathbf{q}}(t) = \mathbf{A}_{ss}\mathbf{q}(t). \tag{10}$$

The system matrix in (10) contains the poles $\lambda_k = -\xi_k\omega_{\mathrm{n},k} \pm \mathrm{i}\omega_{\mathrm{d},k}$, with the damped natural angular frequencies $\omega_{\mathrm{d},k} = \omega_{\mathrm{n},k}\sqrt{1-\xi_k^2}$, while $\omega_{\mathrm{n},k}$ and $0 < \xi_k < 1$ ($k \in \mathcal{M}$) are the undamped natural angular frequencies and the damping ratios, respectively.

The solution operator can be derived for the vicinity of the actual state by the impulse dynamic subspace using the evident equity $\mathbf{x}(t+\mathrm{d}t+\theta) = \mathbf{x}(t+\theta+\mathrm{d}\theta)$, leading to [14]

$$\mathbf{q}(t+\mathrm{d}t) = \langle \tilde{\mathbf{V}}_{\mathrm{d}}(\theta), \tilde{\mathbf{V}}_{\mathrm{d}}(\theta+\mathrm{d}\theta) \rangle \mathbf{q}(t). \tag{11}$$

2.2. Discrete-Time Formulation

Since all frequency response measurements are collected by using a discrete frequency span $\omega_l = l\Delta\omega$ ($l = 0, 1, 2, \ldots, N_{\mathrm{FRF}}$), where $\Delta\omega = \omega_{\max}/N_{\mathrm{FRF}}$ and the bandwidth is denoted by $\omega_{\max}$, then discretization is performed in the bounded time interval $\theta \in [0, T]$ of the IRF as $\theta_j = j\Delta\theta$ ($j = 0, 1, 2, \ldots, N$). Where the number of time intervals is $N = 2N_{\mathrm{FRF}}$ and the signal length of the discretized IRF is $T = 1/\Delta\omega$ (if $\Delta\omega$ is in Hz). In this sense, the discretized part of (6) is expressed as [14,15]

$$\mathbf{x}_T(t) = \mathbf{G}\mathbf{F}_{-T}(t). \tag{12}$$

In this sense, the so-called Hankel matrix representation of the discrete Green function is [14]

$$\mathbf{G} = \begin{bmatrix} \mathbf{h}_0 & \mathbf{h}_1 & \ldots & \mathbf{h}_N \\ \mathbf{h}_1 & \mathbf{h}_2 & \ldots & \mathbf{h}_{N+1} \\ \vdots & \vdots & \ddots & \vdots \\ \mathbf{h}_N & \mathbf{h}_{N+1} & \ldots & \mathbf{h}_{2N} \end{bmatrix}, \quad \mathbf{F}_{-T}(t) = \begin{bmatrix} \mathbf{F}(t) \\ \mathbf{F}(t-\Delta\theta) \\ \vdots \\ \mathbf{F}(t-(N-1)\Delta\theta) \end{bmatrix}. \tag{13}$$

where the discrete IRF $\mathbf{h}_j = \Delta t\mathbf{h}(j\Delta t)$ can simply be compiled by using *ifft* on the measured FRFs coordinate-pairwise.

Then, SVD is applied to the direct counterpart of the discrete Green function (13) as [14]

$$\mathbf{G}_{\mathrm{d}} = \mathbf{V}_{\mathrm{d}}\mathbf{\Sigma}\mathbf{W}^{\mathrm{H}}, \tag{14}$$

where $\mathbf{V}_{\mathrm{d}}, \mathbf{W} \in \mathbb{R}^{D\times N\times D\times N}$. Only M singular values are taken and listed in $\Sigma = \mathrm{diag}_{m=1}^{M}\sigma_m$. Then, the system matrix can be approximated by using these truncated discrete forms via multiplying the displacement-related $\tilde{\mathbf{V}}_{\mathrm{d}}$ and the velocity-related $\tilde{\mathbf{V}}_{\mathrm{d}}$ singular-IRFs as it was introduced in (10), that is,

$$\mathbf{A}_{ss} = \tilde{\mathbf{V}}_{\mathrm{d}}^{\mathrm{H}}\tilde{\mathbf{V}}_{\mathrm{d}}, \tag{15}$$

Due to the equivalence between the impulse time coordinates θ and ϑ, the velocity-related counterpart of the Green function is computed as $\mathbf{G}'_{\mathrm{d}}(\theta,\vartheta)=\sum_{k=1}^{\infty}\sigma_k\mathbf{V}'_k(\theta)\mathbf{W}_k^{\mathrm{H}}(\vartheta)$ according to (7). Then, the velocity-related singular-IRFs are derived as

$$\tilde{\mathbf{V}}'_{\mathrm{d}}=\mathbf{G}'_{\mathrm{d}}\tilde{\mathbf{W}}\tilde{\mathbf{\Sigma}}^{-1}, \tag{16}$$

where $\mathbf{G}'_{\mathrm{d}}=[\mathbf{G}'_{\mathrm{d},k,l}]=\Delta\theta\{\mathbf{h}'_{\mathrm{d}}((k-1)\Delta\theta+(l-1)\Delta\theta)\}$ and $\mathbf{h}'_{\mathrm{d}}(\theta)=\mathcal{F}^{-1}\{\mathrm{i}\omega\mathbf{H}_{\mathrm{d}}(\omega)\}$.

Based on (11), a discrete map can be derived in the form

$$\mathbf{q}_{j+1}=\mathbf{B}_{ss}\mathbf{q}_j,\quad \mathbf{B}_{ss}=\tilde{\mathbf{V}}_{\mathrm{d}}^{\mathrm{H}}\mathbf{S}\tilde{\mathbf{V}}_{\mathrm{d}},\quad \mathbf{q}_j=\mathbf{q}((j-1)\Delta t), \tag{17}$$

where $\mathbf{S}$ is a shift matrix shifting the discrete array $\tilde{\mathbf{V}}_{\mathrm{d}}$ by one step (with $\Delta\theta=\Delta t$). The eigenvalues μ of the solution map $\mathbf{B}_{ss}$ are in connection with the poles according to $\mu=\mathrm{e}^{\lambda\Delta t}$.

2.3. Applications to Power Systems

The frequency data-based dominant decomposition for power systems procedure is illustrated in Figure 1; its implementation is based on the nonlinear simulation environment of the Power System Toolbox (PST) [16]. The step-by-step execution to gather the multi-input–multi-output (MIMO) data structures is performed as follows:

1. Sequential probing experiments: Rather than exciting all control loops simultaneously, a sequence of independent nonlinear time-domain simulations is carried out column-by-column. For each experiment i (where $i=1,\ldots,n$), a logarithmic chirp perturbation signal $u_i(t)$ is injected exclusively into the reference channel of the i-th generator's AVR with $f_s=0.2$ Hz and $f_e=3$ Hz, according to (2). The remaining $n-1$ excitation inputs are kept inactive.
2. Spatio-temporal data logging: During each simulation run, the dynamic response of the network is recorded over a transient window of 100 s to ensure that the electromechanical transient behavior is fully captured. The spatiotemporal output variables, corresponding to the p rotor speed deviations ($\Delta\omega$), are collected and stored. This creates an experimental output data packet associated with the i-th input channel.
3. MIMO data assembly: Once the n sequential simulation runs are completed, the raw time-domain signals are compiled into the global data structures $\mathbf{u}(t)$ and $\mathbf{y}$. These arrays organize the input–output cross-correlations, establishing the definitive link between the nonlinear multi-machine simulation time series and the discrete frequency-domain estimation block ($\mathbf{H}(\omega)$) via the fft described in the previous section.
4. IRF computation via IFFT: To isolate the pure impulse dynamics required by the realization algorithm, the ifft is applied to the estimated frequency response matrix $\mathbf{H}(\omega)$. This mathematical operation effectively decouples the nonlinear operational effects of the original chirp signal, mapping the system response back into a clean, time-domain MIMO IRF matrix $\mathbf{h}(t)$.
5. Discrete-time Green function assembly: The continuous-time or densely sampled IRF are subsequently re-sampled at a lower rate ($t_j=j\Delta t$) tailored for electromechanical oscillation analysis. These discrete $p\times n$ parameter blocks ($\mathbf{h}_j$) are then systematically and recursively stacked into the so-called Hankel matrix representation of the Green function.
6. System identification ($\mathbf{A}_{ss},\mathbf{B}_{ss},\mathbf{C}_{ss},\mathbf{D}_{ss}$): Finally, the $\mathbf{G}_d$ matrix is factored through a singular value decomposition of rank r. The dominant left and right singular vectors are used to compute the discrete-time matrices $(\mathbf{A}_{ss},\mathbf{B}_{ss},\mathbf{C}_{ss},\mathbf{D}_{ss})$.

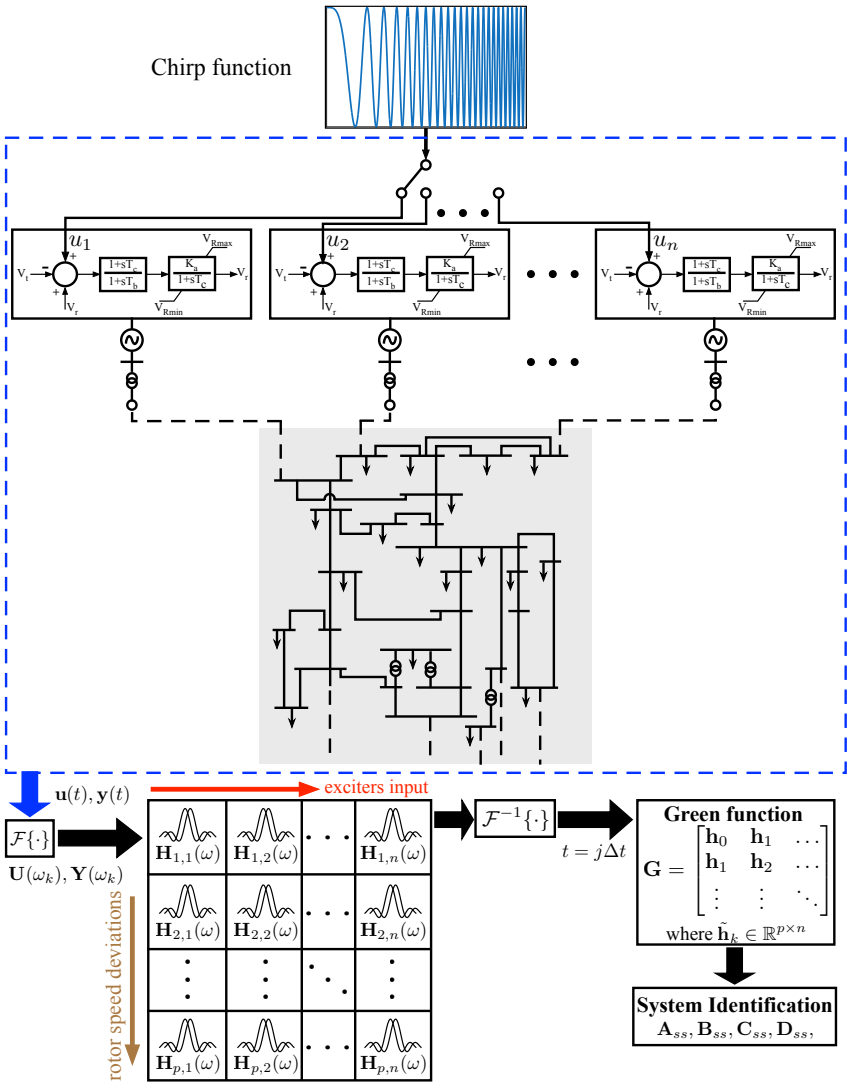

Figure 1. Flowchart of the DMD-assisted linear models for power systems.

3. LQG-Based Wide-Area Damping Control Design on the DMD-Identified Model

This section presents the wide-area damping controller synthesized from the reduced model obtained in Section 2. In this paper, DMD refers to the dominant modal decomposition constructed from FRFs, IRFs, and the retained impulse dynamic subspace. It is not used here as a generic snapshot-only dynamic mode decomposition algorithm. This distinction is relevant because the control-oriented realization used below is obtained from the reduced impulse-dynamic coordinates q_k, not from a snapshot regression operator.

The controller is formulated in discrete time because the identified model is a sampled-data realization and the WADC command is updated at the sampling period T_s. Under the identified linear model and the selected quadratic weights, the linear quadratic Gaussian controller provides an optimal output-feedback law for the adopted stochastic linear-quadratic problem. Its damping effectiveness under nonlinear post-fault responses and operating changes is assessed through time-domain simulations.

For clarity, the LQR, LQE, and LQG have distinct but complementary roles in the proposed controller. The linear quadratic regulator (LQR) is a state-feedback control law that determines the gain K by minimizing a quadratic cost defined by the state and control weighting matrices Q and R, respectively. The linear quadratic estimator (LQE), implemented as a steady-state Kalman estimator, reconstructs the unmeasured reduced state

from the available WAMS measurements and determines the estimator gain L_e based on the process- and measurement-noise covariance matrices W and V. The linear quadratic Gaussian (LQG) controller combines these two components through the separation principle: the LQR computes the damping action using the state estimate supplied by the LQE, resulting in the output-feedback law $\bar{u}_k = -K\hat{\bar{x}}_k$. Thus, the LQR performs optimal regulation, the LQE performs state estimation, and the LQG denotes their integrated output-feedback implementation.

3.1. Control-Oriented Dominant Modal Realization

The solution map $\mathbf{B}_{ss}$ obtained in Section 2 is an autonomous state-transition operator. To avoid conflict with the control-input matrix B_d, this section denotes the same operator as Φ_{ss}. Hence, $x_k \equiv q_k$ and $A_d \equiv \Phi_{ss}$.

The reduced realization is expressed in deviation variables around the pre-disturbance operating point, namely, $\Delta x_k = x_k - x_0$, $\Delta u_k = u_k - u_0$, and $\Delta y_k = y_k - y_0$. The deviation symbol is omitted hereafter for compactness. The control-oriented model is

$$x_{k+1} = A_d x_k + B_d u_k + w_k, \qquad y_k = C_d x_k + v_k, \tag{18}$$

where $x_k \in \mathbb{R}^r$ is the retained dominant-modal state, $u_k \in \mathbb{R}^m$ contains the supplementary AVR inputs, and $y_k \in \mathbb{R}^p$ contains the WAMS measurements used by the estimator. Therefore, $A_d \in \mathbb{R}^{r\times r}$, $B_d \in \mathbb{R}^{r\times m}$, and $C_d \in \mathbb{R}^{p\times r}$. The stochastic terms satisfy $\mathbb{E}[w_k w_k^T] = W \succeq 0$, $\mathbb{E}[v_k v_k^T] = V \succ 0$, and $\mathbb{E}[w_k v_k^T] = 0$.

The input matrix B_d is not inferred from the autonomous solution map A_d. It is obtained from the same input–output frequency responses $H_{q,i}(\omega)$ used in Section 2, where each supplementary AVR probing signal defines one control input channel. For the i-th AVR channel, the sampled impulse-response vector is defined as $g_i(\ell) = \mathcal{F}^{-1}\{H_{\cdot,i}(\omega)\}|_{t=\ell T_s}$, $i = 1, \ldots, m$, where $H_{\cdot,i}(\omega)$ denotes the column of the FRF matrix associated with the i-th supplementary AVR perturbation and $g_i(\ell) \in \mathbb{R}^{n_f}$ is the full sampled response vector at the ℓ-th sampling instant.

The reduced input direction associated with this channel is obtained by projecting the input-induced response onto the retained impulse dynamic subspace:

$$b_i = \tilde{V}_d^H g_i(1), \qquad B_d = \begin{bmatrix} b_1 & b_2 & \cdots & b_m \end{bmatrix}. \tag{19}$$

Here, $\tilde{V}_d \in \mathbb{R}^{n_f\times r}$ is the retained sampled dominant-modal basis, r is the reduced model order, and n_f is the dimension of the full sampled response vector. Equation (19) uses the first discrete Markov parameter of each identified AVR-to-output channel. If a delayed or finite-window Markov representation is used in the implementation, $g_i(1)$ is replaced by the corresponding input-delay-consistent response vector before projection. This construction ensures that the columns of B_d represent the dynamic effect of the supplementary AVR inputs in the reduced dominant-modal coordinates, rather than a purely topological incidence relation. The output matrix is obtained as $C_d = C_{\text{phys}}\tilde{V}_d$, where $C_{\text{phys}} \in \mathbb{R}^{p\times n_f}$ is the measurement-selection matrix associated with the WAMS channels used by the estimator. Since the supplementary AVR signal acts through the exciter and generator dynamics, no direct algebraic feedthrough from the WADC input to the selected WAMS outputs is considered at the adopted sampling period.

$$u_k = \text{col}_{g\in\mathcal{G}_{\text{AVR}}}\left(\Delta V_{\text{ref},g}(k)\right), \tag{20}$$

where $\mathcal{G}_{\text{AVR}}$ denotes the set of generators whose automatic voltage regulators receive supplementary WADC commands, and $m = |\mathcal{G}_{\text{AVR}}|$. In the implemented benchmarks,

$|\mathcal{G}_{\mathrm{AVR}}| = 4$ for the Kundur system and $|\mathcal{G}_{\mathrm{AVR}}| = 16$ for the NEPS-NYPS system. The measured vector used by the estimator is selected from the available WAMS channels. For the two-area Kundur system, these channels can include monitored tie-line active-power deviations and inter-area speed differences.

$$y_k^{\mathrm{mon}} = \mathrm{col}_{s\in\mathcal{S}_{\mathrm{WAMS}}}(\Delta y_s(k)), \tag{21}$$

where $\mathcal{S}_{\mathrm{WAMS}}$ denotes the set of monitored tie-line power, speed-difference, frequency, or voltage channels retained for damping assessment. The estimator input is $y_k = S_{\mathrm{sel}} y_k^{\mathrm{mon}}$, where $\mathcal{S}_{\mathrm{WAMS}}$ denotes the available monitored-channel set and S_{sel} is the binary selection matrix defining the channels supplied to the implemented LQE. Speed or frequency-difference channels may be appended when they are part of the implemented measurement set and improve observability of the target inter-area modes.

The vector y_k contains the measured channels used by the estimator, $z_k = C_z \bar{x}_k$ contains the variables weighted in the LQR cost, and $\mathcal{L}$ contains the outputs used for time-domain validation. These sets may overlap, but they need not be identical.

To avoid unit-dependent tuning, the variables are normalized as $\bar{x}_k = S_x^{-1} x_k$, $\bar{u}_k = S_u^{-1} u_k$, and $\bar{y}_k = S_y^{-1} y_k$, where S_x, S_u, and S_y are diagonal scaling matrices. The entries of S_u are selected from the admissible supplementary AVR limits, and the entries of S_y are selected from representative magnitudes of the measured WAMS channels. The normalized realization is

$$\bar{x}_{k+1} = \bar{A}_d \bar{x}_k + \bar{B}_d \bar{u}_k + \bar{w}_k, \qquad \bar{y}_k = \bar{C}_d \bar{x}_k + \bar{v}_k, \tag{22}$$

with $\bar{A}_d = S_x^{-1} A_d S_x$, $\bar{B}_d = S_x^{-1} B_d S_u$, and $\bar{C}_d = S_y^{-1} C_d S_x$. The scaling matrices are fixed before solving the Riccati equations and are kept unchanged during each nonlinear validation case.

3.2. LQR-Based Damping Synthesis

The regulator computes the supplementary damping action by minimizing

$$J_c = \frac{1}{2} \sum_{k=0}^{\infty} \left(\bar{x}_k^T Q \bar{x}_k + \bar{u}_k^T R \bar{u}_k \right), \tag{23}$$

where $Q = Q^T \succeq 0$ penalizes the target oscillatory content and $R = R^T \succ 0$ penalizes the supplementary AVR effort. The full-state LQR law is $\bar{u}_k = -K \bar{x}_k$. In the implemented LQG controller, $\bar{x}_k$ is replaced by its LQE estimate. The gain is

$$K = \left(R + \bar{B}_d^T P \bar{B}_d \right)^{-1} \bar{B}_d^T P \bar{A}_d, \tag{24}$$

and $P = P^T \succeq 0$ is the stabilizing solution of

$$P = \bar{A}_d^T P \bar{A}_d - \bar{A}_d^T P \bar{B}_d \left(R + \bar{B}_d^T P \bar{B}_d \right)^{-1} \bar{B}_d^T P \bar{A}_d + Q. \tag{25}$$

The LQR solution is retained only if $(\bar{A}_d, \bar{B}_d)$ is stabilizable and $(Q^{1/2}, \bar{A}_d)$ is detectable. The weighting matrix Q is connected to the damping objective through the performance output $z_k = C_z \bar{x}_k$:

$$Q = C_z^T W_z C_z + \rho_x I_r, \tag{26}$$

where $W_z \succeq 0$ weights the selected oscillatory variables and $\rho_x > 0$ regularizes non-penalized reduced directions. The vector z_k may include inter-area speed differences, center-of-inertia frequency deviations, or active-power deviations across critical tie-lines.

The effort matrix is selected as $R = \mathrm{diag}(r_1, \ldots, r_m)$, where $r_i > 0$ penalizes the i-th supplementary AVR channel. The LQR determines the full-state damping gain K, whereas the LQE supplies the reduced-state estimate required to implement the output-feedback LQG law $\bar{u}_k = -K\hat{\bar{x}}_k$.

3.3. LQE-Based Wide-Area State Reconstruction

The retained dominant-modal state is not directly measured. A steady-state Kalman estimator estimates its reduced coordinates from the selected PMU/WAMS signals. To avoid ambiguity between predictor–corrector notation and stationary estimator equations, the LQE is written in observer form:

$$\hat{\bar{x}}_{k+1} = \bar{A}_d \hat{\bar{x}}_k + \bar{B}_d \bar{u}_k + L_e(\bar{y}_k - \bar{C}_d \hat{\bar{x}}_k), \tag{27}$$

where $L_e \in \mathbb{R}^{r \times p}$ is the steady-state estimator gain. Let $\Sigma = \Sigma^T \succeq 0$ be the stationary estimation-error covariance associated with the observer form in (27). It is obtained from

$$\Sigma = \bar{A}_d \Sigma \bar{A}_d^T + W - \bar{A}_d \Sigma \bar{C}_d^T \left(\bar{C}_d \Sigma \bar{C}_d^T + V \right)^{-1} \bar{C}_d \Sigma \bar{A}_d^T, \tag{28}$$

and the estimator gain is

$$L_e = \bar{A}_d \Sigma \bar{C}_d^T \left(\bar{C}_d \Sigma \bar{C}_d^T + V \right)^{-1}. \tag{29}$$

The estimator is retained only if $(\bar{A}_d, \bar{C}_d)$ is detectable and $(\bar{A}_d, W^{1/2})$ is stabilizable. The matrix W represents uncertainty in the dominant-modal model and neglected high-order dynamics, while V represents PMU/WAMS measurement uncertainty.

3.4. Integrated Dominant Modal LQG-WADC Implementation

The nominal LQG gains are synthesized from the delay-free reduced realization. Communication delays are subsequently introduced in the WAMS measurement path during nonlinear validation. Hence, the reported delay cases quantify sensitivity of the nominal controller rather than the performance of a delay-compensated LQG design. The LQG controller combines the regulator and estimator through the separation principle. Since the actual reduced state is not measured, the implemented control law is

$$\bar{u}_k = -K\hat{\bar{x}}_k, \qquad u_k = S_u \bar{u}_k. \tag{30}$$

Before being applied to the excitation system, each physical channel is limited as $u_{k,i}^{\mathrm{sat}} = \mathrm{sat}(u_{k,i}, u_i^{\min}, u_i^{\max})$, $i = 1, \ldots, m$. The command injected into the i-th AVR is

$$V_{\mathrm{ref},i}^{\mathrm{cmd}}(k) = V_{\mathrm{ref},i}^{0} + u_{k,i}^{\mathrm{sat}}, \qquad i = 1, \ldots, m. \tag{31}$$

This equation defines the physical interface between the dominant-modal LQG controller and the nonlinear power-system model.

For the unsaturated linear reduced model, the regulator and estimator poles are

$$\lambda_j^{\mathrm{reg}} \in \mathrm{eig}(\bar{A}_d - \bar{B}_d K), \qquad \lambda_j^{\mathrm{est}} \in \mathrm{eig}(\bar{A}_d - L_e \bar{C}_d). \tag{32}$$

The LQG realization is accepted only if

$$|\lambda_j^{\mathrm{reg}}| < 1, \qquad |\lambda_j^{\mathrm{est}}| < 1, \qquad j = 1, \ldots, r. \tag{33}$$

For complex-conjugate regulator poles associated with electromechanical modes, the equivalent damping ratio and modal frequency are

$$\zeta_j^{\mathrm{reg}} = -\frac{\ln|\lambda_j^{\mathrm{reg}}|}{\sqrt{\left(\ln|\lambda_j^{\mathrm{reg}}|\right)^2 + \left(\angle\lambda_j^{\mathrm{reg}}\right)^2}}, \qquad f_j^{\mathrm{reg}} = \frac{\left|\angle\lambda_j^{\mathrm{reg}}\right|}{2\pi T_s}. \tag{34}$$

In the simulations reported in this work, $T_s = 100$ ms is used according to the electromechanical frequency range targeted by the WADC. The controller is not intended to act during the fault inception itself, but to damp the post-fault inter-area oscillatory response after fault clearing.

The admissibility check has two levels. The first level verifies modal displacement and internal stability in the reduced linear model. The second level verifies bounded AVR commands and reduced post-fault oscillations in nonlinear time-domain simulations. The controller tuning $\theta = \{Q, R, W, V\}$ is retained when

$$\Theta_{\mathrm{adm}} = \left\{\theta : \zeta_j^{\mathrm{reg}}(\theta) > \zeta_j^{\mathrm{ol}},\ \forall j \in \mathcal{M};\quad T_\ell^{\mathrm{cl}}(\theta) < T_\ell^{\mathrm{ol}},\ \forall \ell \in \mathcal{L};\quad \|u_i(k;\theta)\|_\infty \le u_i^{\max},\ \forall i\right\}. \tag{35}$$

Here, $\mathcal{M}$ is the set of targeted electromechanical modes, and $\mathcal{L}$ is the set of monitored critical outputs. For the Kundur system, $\mathcal{L}$ includes the monitored tie-line power flows and generator-speed differences. For the NEPS-NYPS system, $\mathcal{L}$ includes the critical inter-area corridors selected from y_k^{mon}. Among the admissible candidates, the selected controller is the one with the largest admissible R-scaling, or equivalently the smallest peak supplementary AVR command, while satisfying Θ_{adm}.

The dimensions r, m, and p, together with the selected actuation channels, WAMS measurements, scaling matrices, and LQG weights, are fixed for each benchmark before solving the Riccati equations. The resulting WADC in Figure 2 follows the sequence: dominant-modal model identification, projection of AVR and WAMS channels onto the retained dynamic subspace, normalization, LQR/LQE synthesis, supplementary AVR command generation, and validation through modal displacement and nonlinear post-fault simulations.

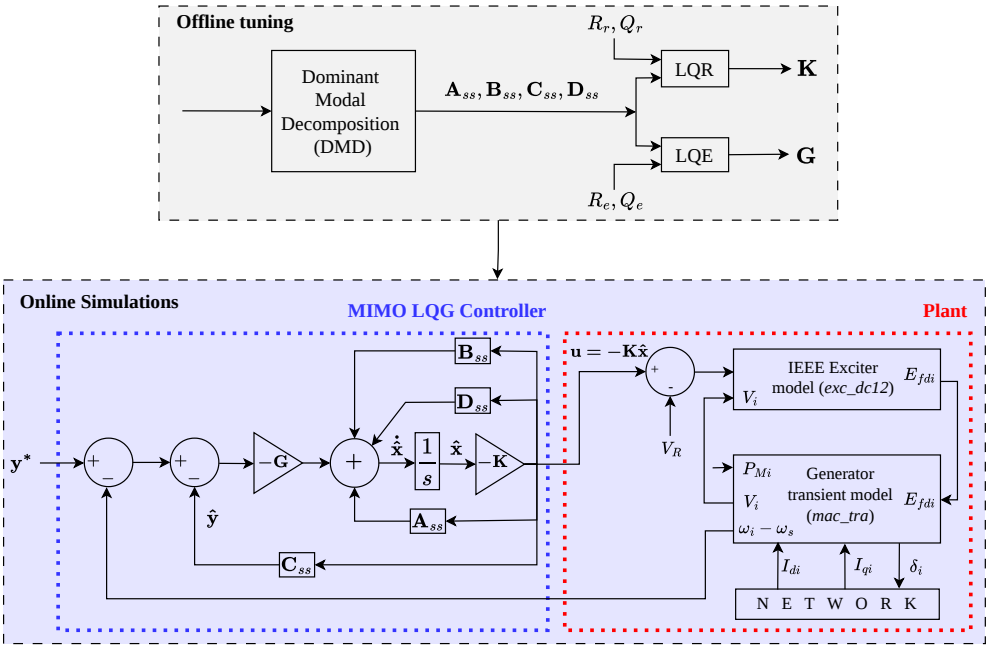

Figure 2. Block diagram for the DMD-integrated WADC.

4. Frequency Data-Based Dominant Decomposition Linear Models for Power Systems

To validate the proposed DMD realization, two well-known benchmark systems are used: (i) the Kundur system and (ii) the New England 68-bus and 16-machine system, both of them have been extensively employed to evaluate methods for small-signal analysis [17].

4.1. Kundur System Identification

Figure 3 illustrates the 14-bus Kundur system representing a two-area power system with two generators in each area. Table 1 summarizes the eigenvalues of the linearized model of the NEPS-NYPS system obtained with the proposed method and for comparison, with the well-known small-signal analysis (SSA). Notice that the last column in Table 1 shows the relative errors between the frequencies and damping ratios obtained with the proposed DMD method and the accurate values obtained with SSA, ϵ_f and ϵ_{dr}, respectively, which are very small for the frequencies and less than 1% for the damping ratio of the inter-area mode.

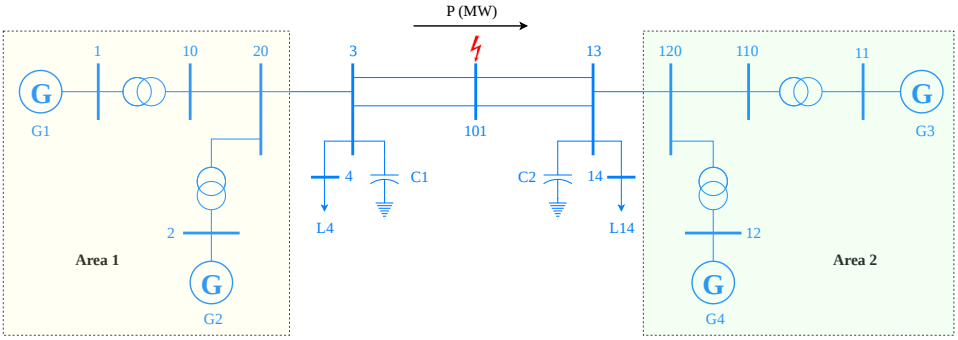

Figure 3. One-line diagram for the two-area Kundur system.

Table 1. SSA and DMD for electromechanical oscillating modes of the Kundur system.

SSA		DMD		Relative Errors	
Frequency (Hz)	Damping Ratio (%)	Frequency (Hz)	Damping Ratio (%)	ϵ_f (%)	ϵ_{dr} (%)
±0.61277	6.7156	±0.61011	6.7784	0.4342	0.9340
±1.1573	19.202	±1.1669	17.346	0.8318	9.6639
±1.1777	18.658	±1.1857	17.037	0.6762	8.6895

Figure 4 illustrates the mode shapes of the inter-area mode obtained with DMD and compared with SSA, where generators G1 and G2 in Area 1 swing against generators G3 and G4 in Area 2 in the 0.61 Hz inter-area mode.

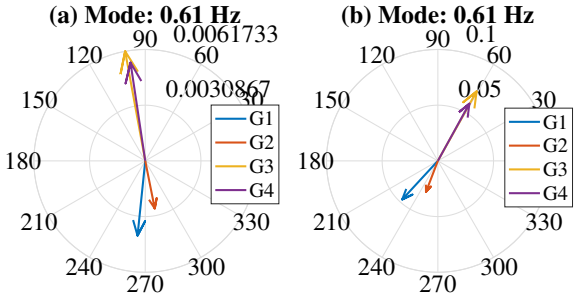

Figure 4. Mode shapes at 0.61 Hz for the Kundur system: (**a**) SSA- and (**b**) DMD-based methods.

Finally, Figure 5 displays the oscillatory modes provided by the SSA and DMD approaches within the frequency range from 0.2 up to 2 Hz, where the DMD approach, indicated by △ can identify all the oscillatory modes of the actual system derived from the SSA-based model, which is symbolized by □.

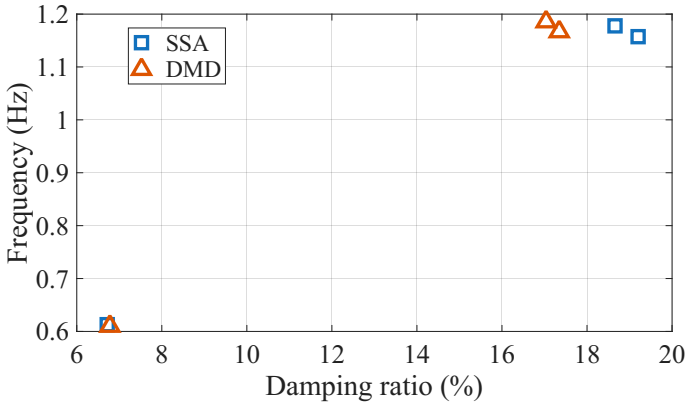

Figure 5. Oscillatory mode behavior over the frequency range 0.2–2 Hz for the Kundur power system.

4.2. New England–New York Power System Identification

The system in Figure 6 consists of a reduced model of the interconnection between New England, which forms area 1, and New York, which is area 2. Areas 3 to 5 are the interconnections with the Ontario Hydro, MISO, and PJM power systems. The reduced system comprises 68 buses and 16 synchronous machines with their excitation systems. The second test is carried out on the benchmark model NEPS-NYPS. Thus, Table 2 shows the eigenvalues of the linearized model of the NEPS-NYPS power system obtained with the proposed method and compared with SSA, where the relative errors ϵ_f and ϵ_{dr} are presented in the last columns. In this case, a maximum relative error in frequency of 3.96% is obtained for the 0.52 Hz inter-area mode and a maximum relative error in damping ratio of 13% for the 0.39 Hz inter-area mode.

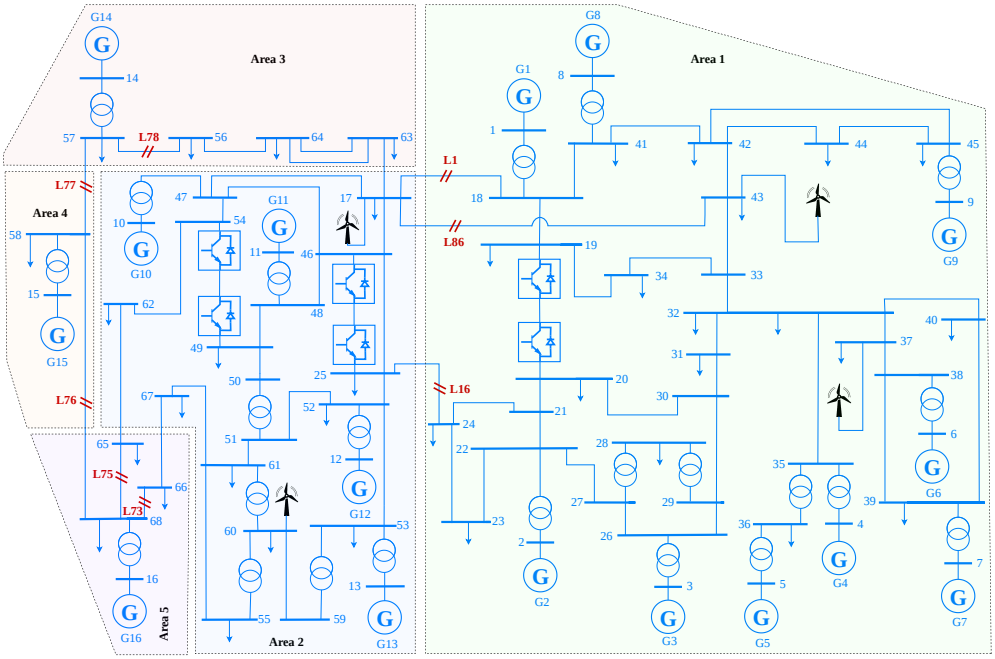

Figure 6. Electric power system representing the NEPS-NYPS model with 68-bus, 16-synchronous generators, 4 WPPs, and 3 HVDC lines.

On the other hand, Figure 7 illustrates the mode shapes for the inter-area modes provided by DMD and compared with SSA, where the lowest oscillatory mode shape has the generators in areas 1 and 2 oscillating against the generators in areas 3, 4, and 5. In the second mode, generator 14 and area 1 oscillate against generator 16. The third mode shape has the generators of area 1 oscillating against area 2. The final mode has generator 15 swinging against generators 14 and 16.

Table 2. SSA and DMD for inter-area oscillating modes of the NEPS-NYPS system.

SSA		DMD		Relative Errors	
Frequency (Hz)	**Damping Ratio (%)**	**Frequency (Hz)**	**Damping Ratio (%)**	ϵ_f (%)	ϵ_{dr} (%)
±0.39889	6.631	±0.39448	7.548	1.1074	13.8301
±0.52637	1.0467	±0.5055	1.0413	3.9653	0.5194
±0.69493	3.5941	±0.69731	3.5711	0.3429	0.6421
±0.79401	3.9543	±0.79212	4.2178	0.2381	6.6629

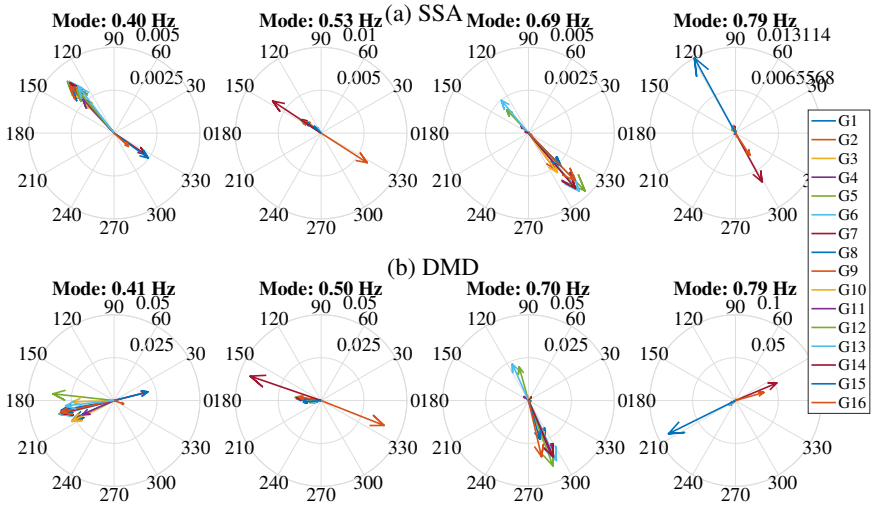

Figure 7. Mode shapes of the inter-area modes for the NEPS-NYPS system: (**a**) SSA- and (**b**) DMD-based methods.

In Figure 8, the oscillatory modes provided by the SSA and DMD approaches within the frequency range from 0.2 up to 1.4 Hz are illustrated, where the DMD approach, indicated by △ can identify all the oscillatory modes of the actual system derived from the SSA-based model, which is symbolized by □.

Finally, the dimensions of the matrices for the Kundur and NEPS-NYPS power systems are summarized in Table 3.

Table 3. Dimensions of the matrices involved in the frequency data-based dominant decomposition linear models derived for Kundur and NEPS-NYPS grids.

Test System	$\mathbf{H}(\omega)$	Order (r)	$\mathbf{G}$	$\mathbf{A}_{ss}$	$\mathbf{B}_{ss}$	$\mathbf{C}_{ss}$	$\mathbf{D}_{ss}$
Kundur	$\mathbb{C}^{4\times4\times16385}$	14	$\mathbb{R}^{1600\times1600}$	$\mathbb{R}^{14\times14}$	$\mathbb{R}^{14\times4}$	$\mathbb{R}^{4\times14}$	$\mathbb{R}^{4\times4}$
NEPS-NYPS	$\mathbb{C}^{16\times16\times16385}$	38	$\mathbb{R}^{2576\times2576}$	$\mathbb{R}^{38\times38}$	$\mathbb{R}^{38\times16}$	$\mathbb{R}^{16\times38}$	$\mathbb{R}^{16\times16}$

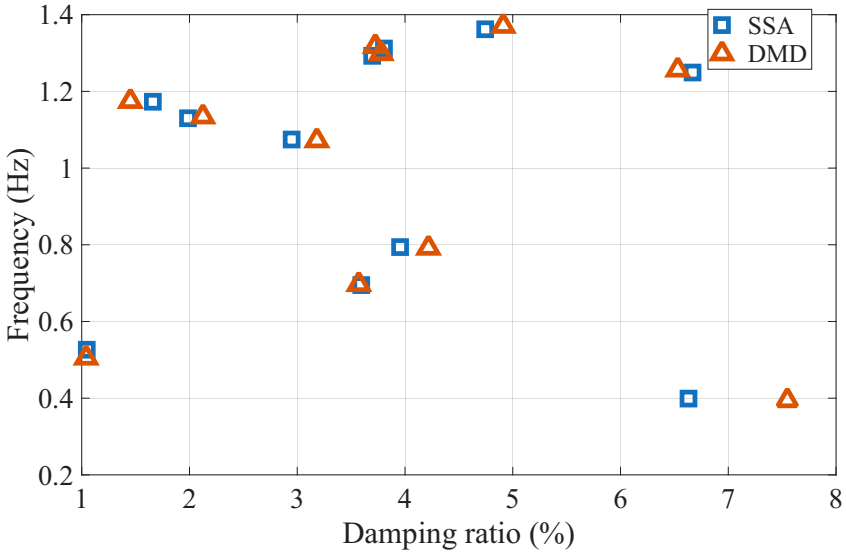

Figure 8. Oscillatory mode behavior over the frequency range 0.2–2 Hz for the NEPS-NYPS power grid.

5. Wide-Area Damping Control Performance

To assess the performance of the proposed wide-area damping control strategy, the 14-bus Kundur and 68-bus NEPS-NYPS systems are used. For both systems, nonlinear simulations are performed for 25 s with a time step of 100 ms. The whole implementation of the proposal is publicly available online in [18].

5.1. Kundur System

In this system, a time-domain simulation is carried out by applying a three-phase short-circuit fault at bus 101. The fault is initiated at $t = 1.0$ s and lasts for six cycles, producing a large disturbance, as shown in Figure 9. In this figure, it can be observed that real power reaches variations above 3 pu, which are mitigated approximately at 10 s without the controller implemented.

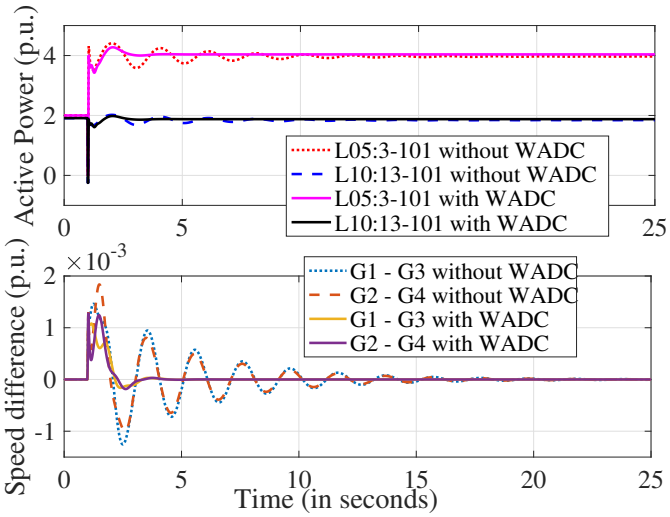

Figure 9. Behavior of real power flows through the tie-lines among areas in the Kundur grid without and controlling four AVRs with the proposed WADC.

Then, the data-driven wide-area control is evaluated by including the DMD identification method and the LQG-based control. In each generator's voltage regulator, an additional input is added to control the response of each generator against the disturbance,

and the response of the system is illustrated by the tie-line active power flows between areas in Figure 9. It can be observed that the power-flow oscillation is damped out in less than 6 s, demonstrating the efficacy of the DMD-assisted WADC scheme.

A sensitivity analysis is performed, introducing latency into the system's measured signals. Communication system latency can significantly affect the damping performance and stability of power systems. Oscillation controllers rely on measurements of system variables to generate control actions. When latency is introduced through different mechanisms, such as sensing, communication networks, signal processing, or controller computation, the control action is applied with a delay relative to the actual system dynamics. This delay could create an additional phase lag that, if sufficiently large, may shift the closed-loop poles toward instability. In this case, the time delay in the communication process includes the serial delay (Ts), the packet delay (Tb), the propagation delay (Tp), and the routing delay (Tr), as is presented in [19]:

$$T_l = T_s + T_b + T_p + T_r \tag{36}$$

The system dynamic response under latency variation (D_{rt}) varying from 50 ms to 300 ms in the signal associated with the generator rotor speed (ω_i) in the Kundur system is presented in Figure 10. Even as the time latency increases, the active power flow through line 5, which connects buses 3 and 101, does not show significant changes, despite the response being delayed by the incorporated latency. This reflects that the identification and control of the system are able to manage these types of communication issues.

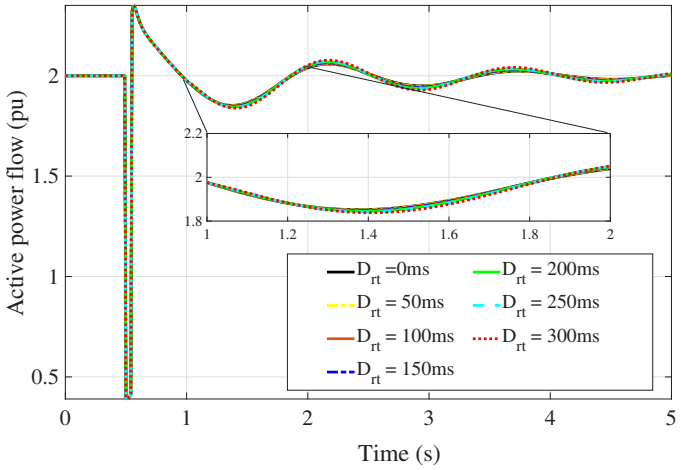

Figure 10. Impact of the latency in communication channels (ranging from 50 ms to 300 ms) in the Kundur system by using the proposed DMD-assisted WADC.

5.2. New England–New York Benchmark Power Grid

The second benchmark used to test the performance of the proposed WADC strategy is the NEPS-NYPS [17], as this system is larger than the Kundur system and exhibits several inter-area modes across the different areas.

After tuning the controller following the proposed WADC methodology, a disturbance is created in the nonlinear NEPS-NYPS model, which consists of a six-cycle three-phase fault at bus 32 (Medway substation). Then, after the fault, the active power flows are monitored in the tie-lines consisting of three AC transmission lines (L01, L86, and L16) interconnecting buses 17-18, 17-43, and 25-24, respectively; two AC transmission lines (L77 and L78) interconnecting buses 57-56 and 57-58; and one AC transmission line (L76) connecting nodes 68-58. The active power of these lines is shown in Figure 11, where the most prominent oscillations before the implementation of the WADC controller, with the

most extended duration, are presented in lines L1: 17-18 and L16: 25-24; and line L73: 68-66 presents the largest amount of transference of active power (about 11 p.u.).

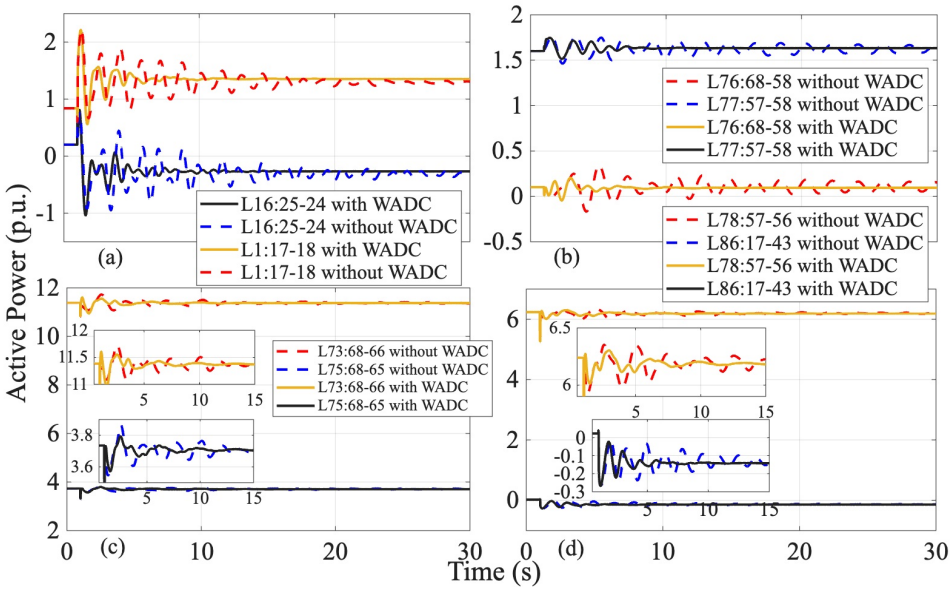

Figure 11. Behavior of real power flows between areas in the NEPS-NYPS grid without and with regulating 16 AVRs with the proposed WADC through the tie-lines. (**a**) L1 and L16. (**b**) L76 and L77. (**c**) L73 and L75. (**d**) L78 and L86.

5.3. Adding 30% Wind Generation and HVDC Lines to the NEPS-NYPS Grid

To assess the performance of the WADC control strategy and verify its applicability to systems with power electronics devices, the flowchart in Figure 2 is applied to the same NEPS-NYPS system but incorporating wind power plants and HVDC lines. The HVDC lines replace the line interconnections of buses 25 and 46, 19 and 20, and 49 with 54, and the WPPs are added to buses 17, 37, 43, and 60, as presented in Figure 6.

The WPP model used in the simulations is type 3, consisting of a double-fed induction generator, with 30% of the power fed to the grid via the converter and the remainder through the direct connection point. The wind power plants are set to operate with an active power dispatch of 100 MW and a unity power factor. As in the previous cases, the WADCs are implemented as voltage references for the AVRs on the synchronous generators. A three-phase fault is also applied to the system with the WPPs and HVDC, and the response is shown through the active power flow in the lines connecting the different areas in Figure 12. The WADC strategy operates effectively, mitigating oscillations in the system and reducing the settling time up to less than 10 s, even when the incorporated WPPs and HVDC line already have a damping effect on the oscillations. This result demonstrates a suitable performance of the WADC in response to changes in operating conditions and topology.

Finally, a sensitivity analysis is performed in the NEPS-NYPS system with 30% wind generation and HVDC links. The WADC is evaluated with round-trip delays introduced into the synchronous-generator rotor-speed measurement channels, as in the Kundur case. Figure 13 shows the active power flow in line L1 (17–18) for delay values ranging from 50 to 150 ms. As the delay increases, the oscillations also increase; however, the WADC mitigation effect remains evident, and the settling time remains below 10 s.

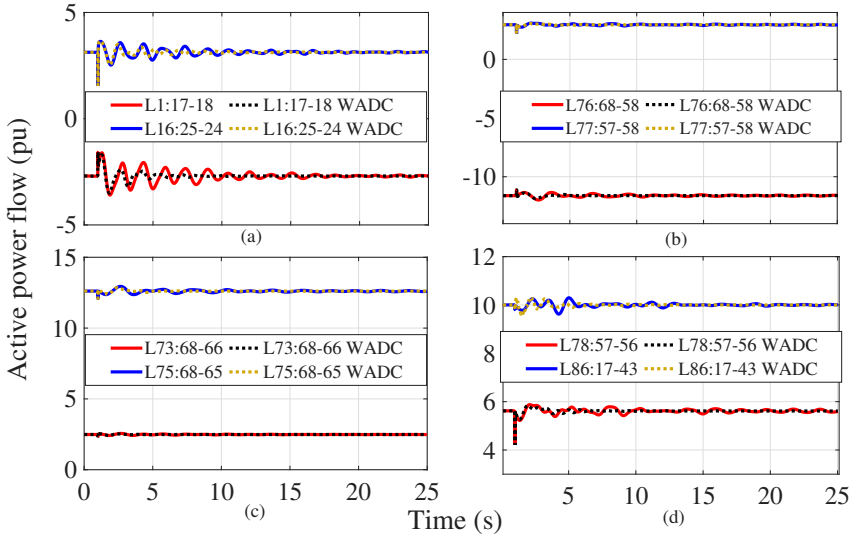

Figure 12. Behavior of real power flows between areas in the NEPS-NYPS grid when adding 30% of wind generation and HVDC lines, with and without regulating 16 AVRs with the proposed WADC through the tie-lines. (**a**) L1 and L16. (**b**) L76 and L77. (**c**) L73 and L75. (**d**) L78 and L86.

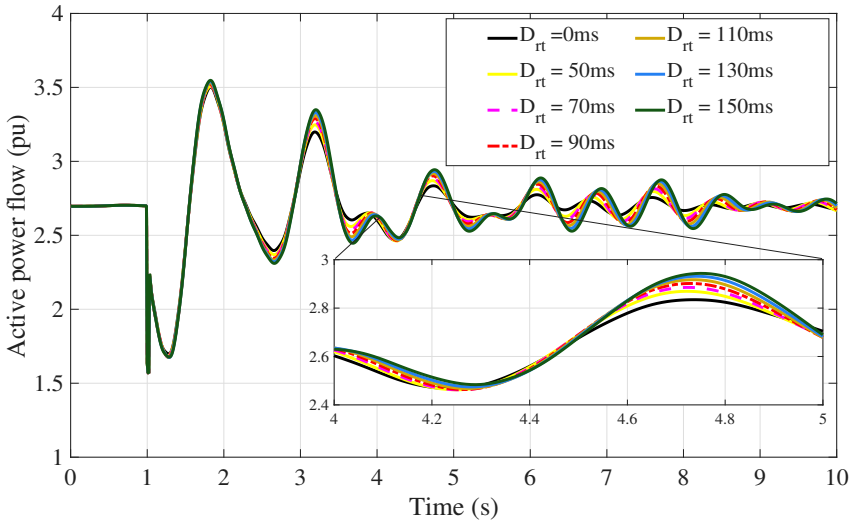

Figure 13. Impact of the latency (ranging from 50 ms to 150 ms) in the proposed WADC in the NEPS-NYPS system with the presence of WPPs and HVDC lines.

6. Conclusions

By projecting the AVR excitation channels and output measurements onto the retained impulse-dynamic subspace, the proposed identification technique successfully bypasses the requirement for full dynamic network parameters while preserving an exact physical mapping of the dominant oscillatory modes. Furthermore, comparative evaluations against SSA demonstrate that this data-assisted realization captures inter-area and local modal frequencies and damping ratios with higher precision, while accurately reconstructing the mode shapes and spatial dynamic activity across the power grid. As a result, the extracted subspace provides a clear, control-oriented state-space model directly from multichannel WAMS measurements.

The attained results demonstrate that the proposed dominant modal realization supports coordinated wide-area damping synthesis in addition to modal assessment. In the Kundur system, the discrete-time LQG controller uses four supplementary AVR channels to attenuate the post-fault tie-line power and inter-area speed responses, with the reported power-flow oscillations damped in less than 6 s. The same architecture is extended to

the NEPS-NYPS benchmark through sixteen AVR channels and multiple monitored inter-area corridors. Together, the modal-displacement results and nonlinear fault simulations indicate that the FRF/IRF-derived dominant subspace captures the control-relevant dynamics required for output-feedback WADC synthesis in an interpretable control-oriented representation. The Kundur latency study further shows that the reported line-flow response remains qualitatively preserved for communication delays from 50 to 300 ms. These results demonstrate that the proposed DMD–LQG framework provides a transparent measurement-derived route for coordinated AVR-based damping, while broader validation under operating-point uncertainty, packet losses, and larger communication disturbances remains necessary.

Even with the addition of rotor-angle signal latency in the synchronous generators, the WADC implemented in both systems still dampens oscillations, proving suitable performance under unfavorable operating conditions. However, it is important to consider that the good response of this control to delay is largely due to the accurate identification of the oscillatory modes using the DMD method.

In the second scenario of the NEPS-NYPS, which adds wind power plants and an HVDC line, the WADC strategy enhances the system's ability to respond to external disturbances. This improvement occurs because the initial identification detects the inter-area modes that influence the system; thus, even with these mitigating elements in place, the control effectively dampens oscillations by reducing the settling time and overshoot magnitude.

Author Contributions: Conceptualization, M.R.A.P., P.M.V., A.Z.-M., C.C.-F., G.E.M.-R. and A.V.-I.; Methodology, M.R.A.P., G.L.R., P.M.V. and A.Z.-M.; Software, G.L.R., A.Z.-M. and C.C.-F.; Formal analysis, M.R.A.P., G.L.R., P.M.V., A.Z.-M., C.C.-F., G.E.M.-R. and A.V.-I.; Investigation, M.R.A.P., G.L.R., P.M.V., A.Z.-M., A.P., C.C.-F., G.E.M.-R., A.V.-I., F.R.S.S. and P.K.; Writing—original draft, M.R.A.P., G.L.R., P.M.V., A.Z.-M., A.P. and C.C.-F.; Writing—review & editing, M.R.A.P.; Visualization, A.P., F.R.S.S. and P.K.; Supervision, M.R.A.P., P.M.V. and A.Z.-M. All authors have read and agreed to the published version of the manuscript.

Funding: This research received no external funding.

Data Availability Statement: The original contributions presented in the study are included in the article, further inquiries can be directed to the corresponding author.

Acknowledgments: M.R.A. Paternina acknowledges support from the Support Program for the Improvement of Academic Staff of UNAM (DGAPA, PASPA-2026). A. Zamora from the Universidad Michoacana acknowledges the support provided by CONAHCYT through Project CF-2023-I-1174 within the framework of the Ciencia de Frontera 2023.

Conflicts of Interest: The authors declare no conflicts of interest.

References

1. Klein, M.; Rogers, G.J.; Kundur, P. A Fundamental Study of Inter-Area Oscillations in Power Systems. *IEEE Trans. Power Syst.* **1991**, *6*, 914–921. [CrossRef]
2. Zenelis, I.; Wang, X. A Model-Free Sparse Wide-Area Damping Controller for Inter-Area Oscillations. *Int. J. Electr. Power Energy Syst.* **2022**, *136*, 107609. [CrossRef]
3. Benasla, M.; Berkani, A.; Bouchenafa, I.; Allaoui, T.; Korba, P.; Segundo Sevilla, F.R.; Ramirez-Gonzalez, M. Robust Input/Output Signal Selection for WADCs: Comparing Independent and Parallel Operation with Local PSSs. *Energies* **2026**, *19*, 954. [CrossRef]
4. Bhadu, M.; Senroy, N.; Kar, I.N.; Sudha, G.N. Robust Linear Quadratic Gaussian-Based Discrete Mode Wide Area Power System Damping Controller. *IET Gener. Transm. Distrib.* **2016**, *10*, 1470–1478. [CrossRef]
5. Bento, M.E.C. A New Method to Design Resilient Wide-Area Damping Controllers for Power Systems. *Energies* **2025**, *18*, 5323. [CrossRef]
6. Prakash, A.; Kumar, K.; Parida, S.K. A Modal Transformation Approach to Design Reduced Order Functional Observer-Based WADC for Low-Frequency Oscillations. *IEEE Trans. Power Syst.* **2023**, *38*, 3593–3604. [CrossRef]

7. Prakash, A.; Kumar, K.; Parida, S.K. Energy Capacitor System Based Wide-Area Damping Controller for Multiple Inter-Area Modes. *IEEE Trans. Ind. Appl.* **2022**, *58*, 1543–1554. [CrossRef]
8. Prakash, A.; El Moursi, M.S.; Parida, S.K.; El-Saadany, E.F. Design of Adaptive Damping Controller With Wide-Area Measurements Considering Unknown Power System Dynamics. *IEEE Trans. Power Syst.* **2024**, *39*, 5150–5162. [CrossRef]
9. Fank, D.; Renner, H. Enhancement of Inter-Area Oscillation Damping by Wide-Area Controlled Hydropower Plants. *IET Gener. Transm. Distrib.* **2023**, *17*, 762–774. [CrossRef]
10. Zolotas, A.C.; Chaudhuri, B.; Jaimoukha, I.M.; Korba, P. A Study on LQG/LTR Control for Damping Inter-Area Oscillations in Power Systems. *IEEE Trans. Control Syst. Technol.* **2007**, *15*, 151–160. [CrossRef]
11. Prakash, A.; El Moursi, M.S.; Parida, S.K.; Tiwari, R.K. Adaptive Unscented Filtering Based Decoupled Wide-Area Damping Controller for Power Systems. *IEEE Trans. Power Syst.* **2026**, *41*, 29–42. [CrossRef]
12. Zenelis, I.; Wang, X.; Kamwa, I. Online PMU-Based Wide-Area Damping Control for Multiple Inter-Area Modes. *IEEE Trans. Smart Grid* **2020**, *11*, 5451–5461. [CrossRef]
13. Mejia-Ruiz, G.E.; Cárdenas-Javier, R.; Arrieta Paternina, M.R.; Rodríguez-Rodríguez, J.R.; Ramirez, J.M.; Zamora-Mendez, A. Coordinated Optimal Volt/Var Control for Distribution Networks via D-PMUs and EV Chargers by Exploiting the Eigensystem Realization. *IEEE Trans. Smart Grid* **2021**, *12*, 2425–2438. [CrossRef]
14. Dombovari, Z. Dominant modal decomposition method. *J. Sound Vib.* **2017**, *392*, 56–69. [CrossRef]
15. Proctor, J.L.; Brunton, S.L.; Kutz, J.N. Dynamic mode decomposition with control. *SIAM J. Appl. Dyn. Syst.* **2016**, *15*, 142–161. [CrossRef]
16. Chow, J.H.; Cheung, K.W. A toolbox for power system dynamics and control engineering education and research. *IEEE Trans. Power Syst.* **1992**, *7*, 1559–1564. [CrossRef]
17. Canizares, C.; Fernandes, T.; Geraldi, E.; Gerin-Lajoie, L.; Gibbard, M.; Hiskens, I.; Kersulis, J.; Kuiava, R.; Lima, L.; DeMarco, F.; et al. Benchmark models for the analysis and control of small-signal oscillatory dynamics in power systems. *IEEE Trans. Power Syst.* **2017**, *32*, 715–722. [CrossRef]
18. Camila Castrillon, A.Z.M.; Paternina, M.R.A. Power Oscillation Damping Controller Powered by Data-Assisted Dominant Modal Decomposition. Available online: https://github.com/mcamicast/DMD_ERA_Files (accessed on 1 September 2026).
19. Sharma, I.; Cañizares, C.; Bhattacharya, K. Smart Charging of PEVs Penetrating Into Residential Distribution Systems. *IEEE Trans. Smart Grid* **2014**, *5*, 1196–1209. [CrossRef]

Disclaimer/Publisher's Note: The statements, opinions and data contained in all publications are solely those of the individual author(s) and contributor(s) and not of MDPI and/or the editor(s). MDPI and/or the editor(s) disclaim responsibility for any injury to people or property resulting from any ideas, methods, instructions or products referred to in the content.